Boundary-Layer Meteorology manuscript No.
(will be inserted by the editor)

Turbulent inflow precursor method with time-varying direction for large-eddy simulations and applications to wind farms

Wim Munters · Charles Meneveau · Johan Meyers

Received: DD Month YEAR / Accepted: DD Month YEAR

Abstract A major challenge in turbulence-resolving flow simulations is the generation of unsteady and coherent turbulent inflow conditions. Precursor methods have proven to be reliable inflow generators but are limited in applicability and flexibility especially when attempting to couple boundary-layer dynamics with large-scale temporal variations in the direction of the inflow. Here, we propose a methodology that is capable of providing fully developed turbulent inflow for time-varying mean-flow directions. The method is a generalization of a concurrent precursor inflow technique, in which a fully developed boundary-layer simulation that uses periodic boundary conditions is dynamically rotated with the large-scale wind direction that drives the simulation in the domain of interest. The proposed inflow method is applied to large-eddy simulations of boundary-layer flow through the Horns Rev wind farm when subjected to a sinusoidal variation in wind direction at the hourly time scale.

Keywords Inflow turbulence generation, Large-eddy simulation, Wind energy

W. Munters · J. Meyers (✉)
Department of Mechanical Engineering, KU Leuven, Celestijnenlaan 300A–Bus 2421, B3001 Leuven, Belgium
E-mail: johan.meyers@kuleuven.be

C. Meneveau
Department of Mechanical Engineering, Johns Hopkins University, 3400 North Charles Street, Baltimore, Maryland 21218, USA

1 Introduction

Surface fluxes at the land–atmosphere interface are greatly affected by the flow structures in the turbulent atmospheric boundary layer (ABL) (Stull 1988; Garratt 1994). At large scales, wind farms also exhibit complex interactions with the background ABL flow (see, e.g., Calaf et al. 2010; Lu and Porté-Agel 2011; Calaf et al. 2011; Churchfield et al. 2012a; Meyers and Meneveau 2013; Goit and Meyers 2015) as well as complex wake interactions between individual turbine wakes (Ivanell 2009; Barthelmie et al. 2010; Stevens et al. 2014a). The use of large-eddy simulations (LES) for modelling land–ABL interactions (see, e.g., Moeng 1984; Albertson and Parlange 1999; Bou-Zeid et al. 2005, 2007; Wan and Porté-Agel 2011; Anderson et al. 2012) as well as wind-farm–ABL interactions has been an important contributor to gaining insights into the complex flow physics involved.

In the LES approach, large energy-containing turbulent-flow fluctuations are spatially and temporally resolved in the simulations. These fluctuations are particularly relevant for wind-farm–ABL interactions, as they are the source of many important phenomena critical to wind-farm operation and design, such as increased fatigue loading of the tower and blades, the recovery of turbine wakes by turbulent entrainment of high energy fluid from the shear layer above, and the temporal variability in produced power. Many studies in the field of wind energy have applied LES to canonical wind-farm cases, i.e. with periodic boundary conditions under a constant flow forcing and mean wind direction (see, e.g., Ivanell 2009; Calaf et al. 2010; Porté-Agel et al. 2011). Such simulations are relevant to the asymptotic limit of very large wind farms. However, one is also often interested in entrance effects and the spatial development of the flow in finite-length wind farms. For such simulations, it is necessary to use realistic inflow conditions representing turbulent flow from upstream of a wind farm, unperturbed by the wind turbines (Churchfield et al. 2012a; Stevens et al. 2014b; Mirocha et al. 2014a).

ABL turbulence directly leads to variations in the power produced by a wind turbine. However, when many turbines are distributed over a significant spatial area, these variations tend to be smoothed out, resulting from a limited spatial correlation and relatively small length scale of the turbulent fluctuations. Larger scale transients and fluctuations in wind direction and speed typically originate from mesoscale meteorological processes such as cellular convection and weather fronts (Vincent 2010). These phenomena are characterized by length scales of typically 10 to hundreds of kilometres, with associated time scales of tens of minutes up to several hours (Orlanski 1975; Ray 1986). The related fluctuations in flow conditions are hence highly correlated across the entire wind farm and lead to severe power fluctuations. Porté-Agel et al. (2013) performed a large number of wind-farm LES with different steady mean wind directions, showing that even a slightly different mean wind direction involves significant variation in wake conditions of downstream turbines, which leads to large changes in wind-farm aggregate power output. In order to accurately predict wind-farm power under realistic meteorological conditions it is therefore important to be able to incorporate large-scale mean-flow transients in wind-farm LES.

In this work, we discuss the simulation of finite-length wind farms, with realistic turbulent inflow conditions, subject to transient mean-flow variations at the hourly scale. The importance of generating adequate inflow conditions for turbulence-resolving simulation strategies such as LES is illustrated by the nu-

merous studies devoted to this topic (see, e.g., Araya et al. 2011; Dietzel et al. 2014; Muñoz-Esparza et al. 2015). Turbulent inflow generation methods can be roughly categorized into precursor methods on the one hand and synthetic turbulence methods on the other. Keating et al. (2004) and Tabor and Baba-Ahmadi (2010) provide a detailed overview of turbulent inflow generators for LES, both illustrating the better quality of precursor-generated turbulence over synthetic inflows. The advantages of Navier–Stokes based precursor methods are however constrained by their limited geometric flexibility and inability to cope with transients in the mean-flow direction. To overcome this constraint, we propose a generalization of the classic precursor methodology that allows the generation of turbulent inflow conditions with unsteady mean-flow directions. The method maintains the key advantage of precursor simulation methods, namely to impose fully developed turbulent inflow conditions containing coherent structures, physical phase relationships and non-Gaussian statistics, while still retaining flexibility to dynamically change the flow direction at an affordable computational cost.

The outline of the paper is as follows: Sect. 2 first discusses the LES solver applied here. Section 3 contains a further discussion on turbulent inflow condition techniques as well as a comparative test case illustrating the quality of precursor-generated turbulence. Section 4 elaborates on the proposed concurrent precursor method, and Sect. 5 applies the developed method to a simulation study of the Horns Rev wind farm under time-varying mean-flow directions. Section 6 finally summarizes the methods and results.

2 Large-Eddy Simulation Model

The simulations are performed using the LES code SP-Wind, which has been developed at KU Leuven over recent years (see, e.g., Meyers and Sagaut 2007; Calaf et al. 2010; Goit and Meyers 2015). The governing equations are the filtered incompressible Navier–Stokes momentum and continuity equations for neutral boundary-layer flows, i.e.,

$$\partial_t \tilde{u}_i + \partial_j(\tilde{u}_i\tilde{u}_j) = -\delta_{i1}\partial_1 p_\infty/\rho - \partial_i \tilde{p}' - \partial_j \tau_{ij}^d + f_i, \tag{1}$$

$$\partial_i \tilde{u}_i = 0, \tag{2}$$

where $\tilde{u}_i$ $(i = 1, 2, 3)$ are the velocity field components as represented on the LES grid scale Δ. The subgrid-scale (SGS) stress tensor is defined as $\tau_{ij} = \widetilde{u_i u_j} - \tilde{u}_i\tilde{u}_j$, and its deviatoric component ($\tau_{ij}^d = \tau_{ij} - \tau_{kk}/3$) is modelled with a standard Smagorinsky model (Smagorinsky 1963), using a constant coefficient $C_s = 0.14$. The Smagorinsky length scale λ is damped near the bottom wall to avoid excessive dissipation of kinetic energy using the damping function introduced by Mason and Thomson (1992), i.e., $\lambda(z)^{-n} = [C_s\Delta]^{-n} + [\kappa(z + z_0)]^{-n}$, where $\kappa = 0.4$ is the Von Karman constant, z_0 is the assumed roughness length at the wall and we take $n = 3$. The trace of the SGS stress tensor is absorbed into the filtered modified pressure $p' = \tilde{p}/\rho - p_\infty/\rho + \tau_{kk}/3$. In the precursor simulation (see further discussion below), the flow is forced through the domain with a constant imposed pressure gradient $\partial_1 p_\infty/\rho$. This forcing defines a reference velocity $u_* = -\sqrt{H\partial_1 p_\infty/\rho}$, with H being the height of the simulation domain; length and time scales are non-dimensionalized with H and H/u_* respectively. To simplify notation, the LES filtering "tilde" is omitted hereafter.

The governing equations are discretized using a Fourier pseudo-spectral scheme in the horizontal (x_1,x_2) directions. For non-periodic boundary conditions, a fringe-region technique is employed (see, e.g., Spalart and Watmuff 1993; Lundbladh et al. 1999; Nordström et al. 1999) (see also Sect. 4.1 for further discussion). The vertical direction (x_3) is discretized with a fourth-order energy-conserving finite difference scheme (Verstappen and Veldman 2003), and the top boundary is treated with a free slip condition, leading to zero shear stress and zero vertical velocity, emulating a fixed ABL height at the top of the domain. At the bottom boundary a standard equilibrium wall-stress model is used with prescribed roughness length z_0 (Piomelli and Balaras 2002; Bou-Zeid et al. 2005; Calaf et al. 2010).

Time integration is performed using an explicit four-stage fourth-order Runge–Kutta scheme, in which the timestep is restricted by setting the maximal diffusive and advective Courant–Friedrichs–Lewy numbers equal to 0.4. Continuity is enforced by solving a Poisson equation for the pressure, while Coriolis forces and the resolved effects of molecular viscosity are neglected. Also, thermal and stratification effects are not included, hence all simulations presented here are neutral boundary-layer cases. The non-linear and SGS terms are de-aliased using the 3/2 rule (Canuto et al. 1988). The code is written in Fortran2003 and parallelized using distributed memory MPI processes with a highly scalable pencil grid partitioning method.

The turbines are represented in the simulation domain using an actuator disk model (ADM), in which the effect of a turbine on the flow is parametrized by a thrust force that is oriented perpendicular to the rotor plane (Mikkelsen 2003). This thrust force corresponds to

$$F_t = -\frac{1}{2}\rho C_T' \left\langle \overline{u}_\perp^T \right\rangle_d^2 \frac{\pi}{4} D^2, \tag{3}$$

where $\left\langle \overline{u}_\perp^T \right\rangle_d$ is the local disk-averaged and exponentially time-filtered velocity perpendicular to the rotor plane, D is the rotor diameter, and C_T' is the disk-based thrust coefficient. This force is distributed uniformly over the rotor disk, and filtered subsequently onto the LES grid, using a Gaussian convolution filter kernel. Details on the implementation are found in Calaf et al. (2010) and Meyers and Meneveau (2010, 2013).

3 Turbulent Inflow Conditions: Background And Motivation

Turbulence-resolving simulations of flows where periodic boundary conditions cannot be straightforwardly invoked carry the non-trivial problem of generating realistic turbulent inflow conditions at an acceptable computational cost. The quality of inflow turbulence has a significant influence on flow features throughout the entire simulation domain, especially in the absence of phenomena triggering turbulence development such as large-scale flow separation, transition, or unstable stratification (Keylock et al. 2011). Comprehensive overviews of inlet conditions for LES can be found in Keating et al. (2004) and, more recently, in Tabor and Baba-Ahmadi (2010). Shur et al. (2014) provide an updated view of these methods from the point of view of turbulence generation at the interface between large-eddy simulations and Reynolds-averaged Navier–Stokes simulations for aeronautical applications.

In the remainder of this section, the two mainstream categories for generating turbulent inflow conditions, synthetic turbulence and precursor methods, are briefly elaborated from a wind-farm LES perspective. Furthermore, a qualitative comparison between these approaches is presented, with results advocating the use of precursor inflow methods for the applications to be considered.

3.1 Synthetic Turbulence Generation

In this approach synthetic turbulence is generated from a chosen model, before it is added to a mean inflow profile. The level of complexity of these methods ranges from (possibly filtered) random noise (see, e.g., Klein et al. 2003; Muñoz-Esparza et al. 2015) to advanced models matching physical spectra and moments that are assumed to evolve rapidly enough into realistic turbulence. Instead of random noise, one can consider a sinusoidally varying noise term with one or a few modes only (Mirocha et al. 2014b). Most more advanced synthetic turbulence models rely on the assumption that turbulence can be specified using only low-order or one-point statistics (Keating et al. 2004). Moreover, they assume that mean shear and turbulence can be specified independently, even though LES studies indicate that this might lead to erroneous results (Park et al. 2014; Mehta et al. 2014). The main advantage to most synthetic turbulence models is the low computational overhead compared to the target simulation of interest.

In the context of wind energy and ABL flows, the synthetic turbulence model developed by Mann (1998) is widely used. The model parametrizes the spectral tensor of neutral ABL turbulence. Anisotropy and linear shear are accounted for by applying rapid distortion theory to the Navier–Stokes equations in combination with an eddy-lifetime assumption. Ivanell (2009) applied Mann's model to the LES of two columns of the Horns Rev wind farm with periodic boundary conditions in the spanwise direction. The match with field measurements was relatively poor, with the LES overestimating turbine interaction in fully waked conditions, causing a significant underprediction of power in downstream rows. This effect might be attributed to the fact that synthetic freestream turbulence fails to trigger wake meandering, which alleviates full wake conditions, as suggested by Churchfield et al. (2012b). España et al. (2011) indeed proved that the meandering process is generated by turbulent fluctuations with length scales larger than the rotor diameter, which are difficult to predict using synthetic models (see also Sect. 3.3). Moreover, streamwise vortex structures are known to play a crucial role in vertical entrainment of kinetic energy (Cal et al. 2010; Calaf et al. 2010). Gopalan et al. (2014) constructed a mesoscale–microscale framework for wind energy applications, using the Mann spectral model to seed the mesoscale Weather Research and Forecasting (WRF) model simulations with smaller scale turbulence at the WRF-LES interface.

Storey et al. (2013, 2014) applied the model as a background turbulence generator in a study of dynamically controlled offshore wind turbines and the operation of wind farms subject to extreme coherent gusts. Other recent examples of the application of Mann's model to wind-farm LES can be found in Troldborg et al. (2011); Keck et al. (2013); Breton et al. (2014) and Sarlak et al. (2015).

3.2 Precursor Methods

Precursor methods rely on an auxiliary flow simulation, (direct or large-eddy simulation) on an independent domain for the generation of turbulent inflow conditions. The precursor often simulates a canonical flow case, such as a flat plate boundary layer, channel flow or plane mixing layer, for which periodic boundary conditions in horizontal directions can be invoked. This allows a rapid generation of turbulent structures as they are recycled through the boundary conditions, and the flow reaches a statistically stationary state after a number of flow-through times. This feature is the main reason behind the widespread popularity of periodic boundary conditions in turbulent flow simulations. For example, Spalart (1988) performed pioneering direct numerical simulation (DNS) of a developing turbulent boundary layer by introducing source terms in the governing equations that transformed the original non-periodic problem into a reference frame with periodic boundary conditions. Spalart and Watmuff (1993) modified this approach with the introduction of a so-called fringe region at the outflow boundary of the domain. In this region, artificial force terms were added to nudge the thickness of the boundary layer back to a desired value that could be used at the inlet of the domain.

The advantage of precursor methods is that turbulent inflow conditions are directly generated by the Navier–Stokes equations. This results in superior accuracy and realism over other available methods, as indicated by earlier comparative studies (Keating et al. 2004; Tabor and Baba-Ahmadi 2010). The main disadvantage of precursor methods however is the considerable additional computational cost associated with an extra Navier–Stokes simulation. Note that, although traditional implementations of precursor methods typically generate an independent database of inflow data, concurrent precursor methods (Stevens et al. 2014a,b) and internal recycling methods (Lund et al. 1998; Mayor et al. 2002; Ferrante and Elghobashi 2004; Araya et al. 2009, 2011) allow inflow conditions to be directly transferred to the inlet of the main domain.

Use of precursor methods in LES of ABL flows and finite size wind farms has been increasing in recent years. Park et al. (2014) apply a precursor type approach in order to estimate structural loading of turbines in a stable ABL. They strongly advocate the use of LES-based inflow methods because many of the aforementioned assumptions made in synthetic turbulence models do not hold in atmospheric flows. Wu and Porté-Agel (2011, 2012, 2013, 2015) used precursor simulation techniques in studies on individual wind turbines as well as wind farms. Churchfield et al. (2012b) performed an LES of the Lillgrund offshore wind farm, and attributed a better match with field measurements, in comparison with earlier studies, to the use of precursor-generated inflow turbulence. Stevens et al. (2014a) used a concurrent-precursor formulation to quantify power gains achieved by staggering turbines inside a wind farm.

3.3 Comparison Between Synthetic And Precursor Methods

A qualitative comparison between inflow turbulence derived from periodic simulations and synthetic turbulence methods is performed. A fully developed neutral boundary layer is simulated using a resolution of $24.5 \times 24.5 \times 12.5$ m^3 on a domain of $16\pi \times \pi \times 1$ km^3. The inflow treatments considered are a white noise

perturbation case (WN), a sinusoidal wave perturbation case (WP) , the Mann model for synthetic turbulence (MANN) and a classical periodic case (P). Since the boundary layer is fully developed, the periodic case is equivalent to the use of a precursor simulation. The bulk velocity is the same for every case, with $U_b \approx 21.7$ m s^{-1}. The computational cost of each of the synthetic methods (WN, WP and MANN) is negligible compared to the cost of the main LES. In practice, the precursor method however requires an additional LES, which is typically performed on a domain identical to the main domain (although, in some cases, a smaller domain can be used). This roughly doubles the computational cost compared to a single domain simulation.

The first simulation case (WN) uses simple white noise in space and time as perturbations to each of the velocity components, where the perturbations have a uniform zero-mean distribution. Simulation results were found to be relatively insensitive to the maximum amplitude of the white noise. Here, we show results obtained with a maximum amplitude of 5 m s^{-1}. This method obviously has no direct physical relation to turbulent flow fields and, as is well-known for such inflow conditions, the dissipative action of the SGS model rapidly damps these fluctuations very close to the inflow plane. The second case (WP) uses sinusoidal wave-like perturbations that contain some spatial coherence as opposed to the white noise case. The perturbations have a maximum amplitude of $\pm$ 2 m s^{-1}. At every point, the amplitude varies also sinusoidally in time over a period of 500 s. These values were chosen based upon a study using a similar approach by Mirocha et al. (2014b), where an amplitude of $2 - 3$ m s^{-1} and a sign reversal period of 1000 s was used (note that, considering our relatively high bulk velocity, we halved the period of our sign reversal to avoid a bias to very long structures). The third case (MANN) is a widely used method in the wind energy field, and applies perturbations derived from Mann's uniform shear model of the spectral tensor in neutral ABL flows (Mann 1998). The open source TuGen code (Gilling 2009) is used to generate a spatially coherent field of turbulent fluctuations. The input parameters for the Mann model are the turbulent length scale $L = 33.6$ m and the parameter defining the degree of anisotropy of the generated turbulence $\gamma = 3.9$, as recommended in the IEC 61400-1 standard (International Electrotechnical Comission 2005). The factor scaling the turbulence intensity is chosen as in van der Laan et al. (2014): we take $\alpha\epsilon^{2/3} = 0.3$ m$^{4/3}$s^{-2}, where α is the Kolmogorov constant and ϵ is the viscous dissipation rate of turbulent kinetic energy. The spatial data are subsequently transformed into a time series of inflow data by invoking Taylor's frozen turbulence hypothesis.

Figure 1 contains snapshots of instantaneous streamwise velocity component contours in horizontal planes at a height $z = 100$ m. The synthetic turbulence cases show significant and slow streamwise development of fluctuations, but they are very far from reaching the turbulence levels of the periodic simulation, and they do not reproduce the typical streamwise-elongated turbulent structures characteristic of high-Reynolds number boundary-layer flows. Specifically, it can be seen that the WN case is unable to develop any of the turbulent structures present in the periodic case. Although it is expected that, given a much longer development region, this transition to a fully developed turbulent state will ultimately occur, covering the required domain length would be computationally prohibitive. The cases WP and MANN, on the other hand, do appear to show some of the small-scale flow features similar to the ones in the fully developed periodic (P) simulation. Note that the

three synthetic inflow cases seem to be operating at a lower mean streamwise velocity than the periodic case. This effect is due to the lack of turbulent transport of momentum towards the wall, which causes the boundary-layer profile to revert to a laminar-like state with associated lower velocities near the wall. The flow recovers partially as turbulence develops downstream in the domain. Of the three synthetic cases, the Mann model provides best results, but also this model does not fully reproduce the large-scale structures in the flow.

We provide further evidence of the high quality of precursor-generated turbulent inflow compared to synthetic methods in our simulation setting through comparison of energy spectra. The energy spectra of the streamwise velocity component as a function of spanwise wavenumber at various distances downstream of the inflow boundary are compared to those obtained from a fully developed periodic simulation. Results are shown in Fig. 2. The spectra confirm the impressions obtained from the velocity field snapshots. It can be seen that the WN case starts from a uniform energy distribution across the entire spectrum. At small distances downstream of the inflow boundary, the higher wavenumber components of the perturbations ($k_y z > 5$) are dissipated more quickly than the lower wavenumber components. This effect has often been observed before (Klein et al. 2003; Keating et al. 2004; Rana et al. 2011). However, even in the long development length available in the domain of our test case, the flow is unable to reach fluctuation levels comparable to the periodic case, both for the large (small k_y) and small (large k_y) scale structures in the flow. We note that the situation might be different under convective temperature conditions where shorter development lengths can be expected.

The WP case performs significantly better, with the high wavenumber part of the spectrum approaching the periodic reference after 10 to 15 km (which in itself is still an expensive simulation length in LES). The low wavenumber part of the spectrum however has severe difficulty in catching up to the periodic case. This can be observed by the absence of large-scale turbulent structures in Fig. 1 compared to the low and high speed streaks in the periodic domain. Moreover, the wave-like nature of the perturbations can be easily identified in the spectrum by the presence of distinct peaks at certain wavenumbers (especially near the inflow boundary). Although the strongest effects of these peaks seem to subside as we move downstream in the domain, they do seem to excite other modes, of which the oscillatory effects can still be observed even after 40 km. The wave-like perturbations thus impose a certain bias to the flow which requires very long distances to disappear.

The MANN case finally clearly outperforms the other two synthetic inflow cases. The higher wavenumber part of the spectrum increases in energy rapidly as the flow progresses through the domain, meaning that the fluctuations improve in quality by running them through a Navier–Stokes simulation, as was also reported by Gilling and Sørensen (2011). The larger scale structures however still do not develop quickly, as was also observed in the WP case. The comparison between these example cases therefore motivates the application and further development of precursor simulation methods since, even though they involve considerable additional computational cost, the quality cannot be matched by any of the synthetic inflow methods.

The comparison thus confirms the positive features of precursor methods for spatially developing wind-farm simulations. These are preferred over synthetic

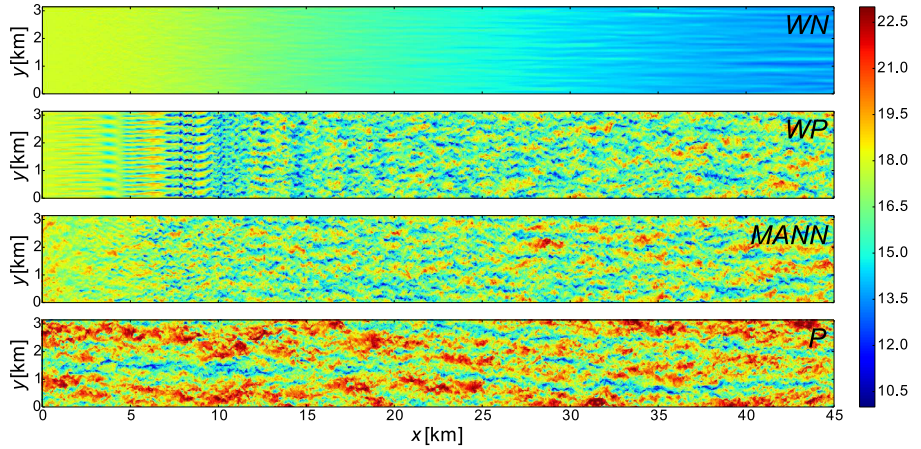

Fig. 1 Instantaneous streamwise velocity component contours at $z/H = 0.1$. Colouring is in units of u/u_*. Four case are considered, from top to bottom: a white noise inflow case (WN), a sinusoidal wave perturbation inflow case (WP), a synthetic "Mann-spectrum" inflow case (MANN), and a fully periodic case (P). The final 10% of the domain in the streamwise direction (including the fringe region) is omitted for clarity.

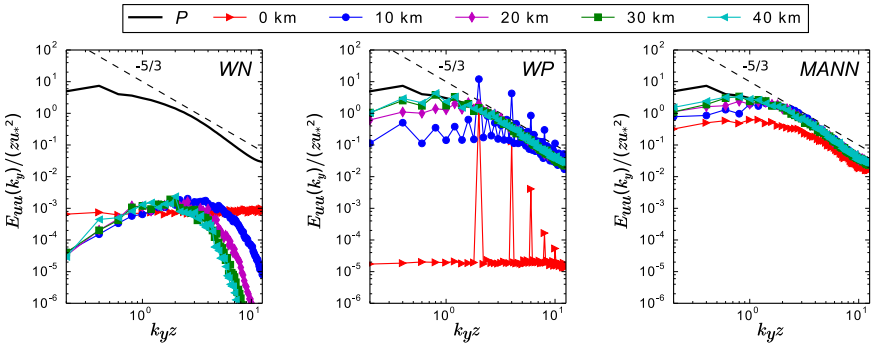

Fig. 2 Streamwise velocity component spectra as a function of spanwise wavenumber at several streamwise locations. Spectra are measured at a height above the wall at $z/H = 0.1$. The black line, identical in every plot, indicates the streamwise-averaged spectrum of the periodic case (P). The cases shown in the panels are, from left to right: a white noise inflow case (WN), a sinusoidal wave perturbation inflow case (WP), and a synthetic "Mann-spectrum" inflow case (MANN).

methods, in particular since the streaky turbulent structure of the ABL can have an important impact on turbine-wake meandering, and the vertical entrainment of kinetic energy.

4 Proposed Variable Inflow-direction Concurrent Precursor Method

Here we present a generalized inflow method, capable of providing fully developed turbulent inflow conditions for varying flow directions. The proposed method uses key features of the concurrent precursor method of Stevens et al. (2014b), in which

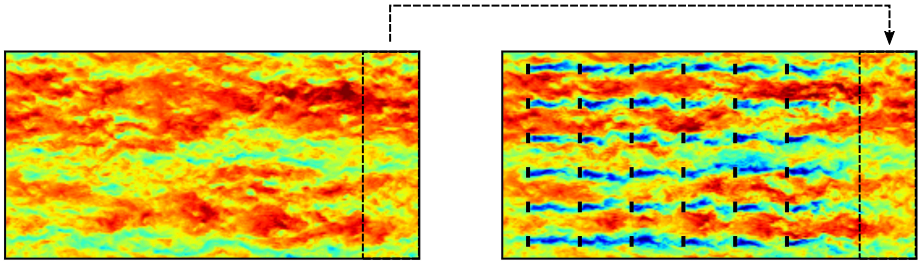

Fig. 3 Illustration of concurrent precursor method from Stevens et al. (2014b) with contours of the streamwise velocity component. *Left:* precursor domain. *Right:* main domain. The dashed lines indicate the start of the inflow data extraction region and the fringe forcing region in the precursor and main domain respectively. The dashed arrow marks the flow of data.

turbulent inflow conditions for a target simulation are derived from an auxiliary flow simulation, running in parallel on an independent domain. The proposed method is also motivated by the limitations of the Stevens et al. (2014b) method that is restricted to a static inflow direction. Hereafter, the target domain is referred to as the *main* domain and the auxiliary domain is referred to as the *precursor* domain. We first elaborate on the mechanism of the original concurrent precursor method and its specific implementation in the SP-Wind solver; afterwards, the generalization to time-varying inflow directions is discussed.

4.1 Stationary Concurrent Precursor Method

The main concept of the concurrent precursor methodology is illustrated in Fig. 3. The precursor domain (illustrated on the left in Fig. 3) applies doubly periodic boundary conditions in the horizontal directions, which facilitates the simulation of fully developed turbulent flow fields. At every timestep, a portion of the precursor flow field is sent over to the back of the main domain (illustrated on the right in Fig. 2). By forcing the flow field in the fringe region of the main simulation to the received values from the precursor and recycling by the periodic boundary conditions, these data are reintroduced as an inflow condition. Both simulations are run synchronously in time using the same timestep. Note that, in theory a single plane of velocity from the precursor simulation would suffice as an inflow condition for the main simulation. Such an approach can be directly used in finite-volume or finite-element discretization methods. However, in the current study, we employ spectral discretization in horizontal planes in combination with a fringe-region method to enforce non-periodic boundary conditions (see further below). In this case, the use of a slab of data that fits the fringe region provides a more gentle transition forcing in the spectral method and avoids spurious pressure gradients in this region. It can be seen from Fig. 3 that the transition of the flow in the fringe region at the end of the main domain towards the desired inflow condition develops very smoothly. Finally, we remark that the flow in the periodic precursor domain is forced with a constant pressure gradient ($-\partial_1 p_\infty$), but this is not necessary in the main simulation domain, in which the flow is forced by the imposed inflow/outflow conditions.

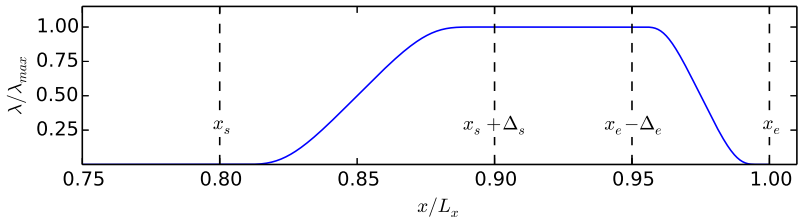

Fig. 4 Example of a fringe masking function $\lambda(x)$, defined by Equation (4b), with parameters $x_s = 0.8L_x$, $x_e = L_x$, $\Delta_s = 0.1L_x$ and $\Delta_e = 0.05L_x$.

In our pseudo-spectral LES method, the main simulation circumvents its periodic boundary conditions through the use of a fringe region technique (Spalart and Watmuff 1993; Lundbladh et al. 1999; Nordström et al. 1999), in which flow variables are smoothly forced to desired inflow values by adding a body force to the governing equations in a so-called "fringe region" at the back of the domain. This allows the entire field to stay periodic while the region of interest (the domain minus the fringe region) is non-periodic.

The fringe force penalizes the error between actual and desired values in the fringe region, and is constructed here as

$$f_{fr,i}(x,y,z) = -\lambda(x)\left[u_i(x,y,z) - u_{prec,i}(x,y,z)\right], \tag{4a}$$

$$\lambda(x) = \lambda_{max}\left\{\mathcal{S}\left(\frac{x-x_s}{\Delta_s}\right) - \mathcal{S}\left(\frac{x-x_e}{\Delta_e}+1\right)\right\}, \tag{4b}$$

$$\mathcal{S} = \begin{cases} 0 & x \le 0 \\ 1/[1+\exp(\frac{1}{x-1}+\frac{1}{x})] & 0 < x < 1 \\ 1 & x \ge 1. \end{cases} \tag{4c}$$

The one-dimensional fringe force masking function λ is non-zero only inside the fringe region part of the domain. A smooth and infinitely differentiable combination of exponentials defined in (4b) – (4c) avoids the introduction of any jump discontinuities, and is therefore amenable to spectral methods without causing spurious Gibbs oscillations. The parameters x_s and x_e set the start and end of the fringe region, while Δ_s and Δ_e provide control over the smoothness of the fringe masking function. Figure 4 illustrates a masking function with typical parameters. The maximum value of the masking function λ_{max} is chosen to be high enough to provide sufficient damping of the flow solution in the fringe region, yet low enough to satisfy the stability constraint $\lambda_{max}\Delta t \le 2.78$ for fourth-order explicit Runge-Kutta time integration without decreasing the timestep (Schlatter et al. 2005). Typical values used for the simulations in this work range from $\lambda_{max} = 1500$ to 3000 for timesteps of the order of $5 \times 10^{-4} H/u_*$.

4.2 Variable Inflow-direction Concurrent Precursor Method

In this subsection the generalization of the precursor methodology to varying inflow directions is presented. In the method, the fully developed periodic boundary-layer (precursor) simulation is dynamically rotated with the (known imposed) flow

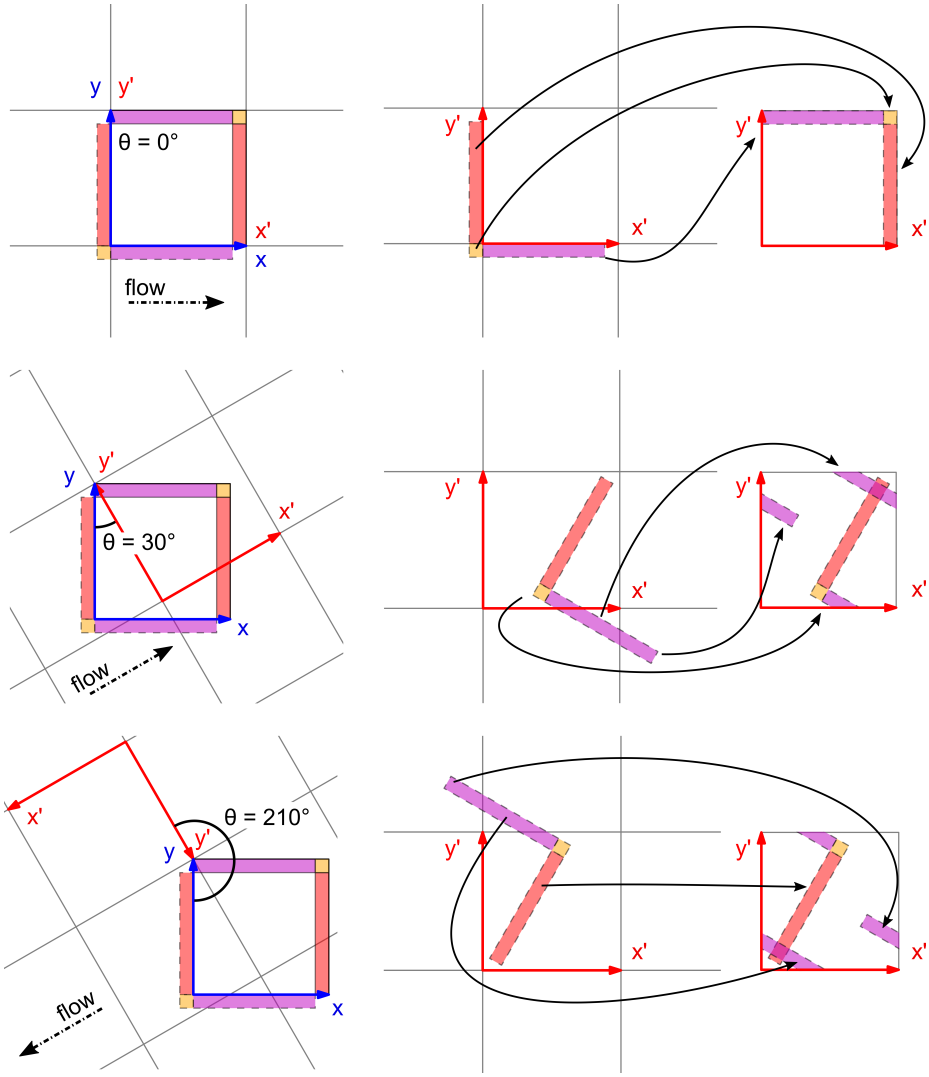

Fig. 5 Illustration of variable-direction concurrent precursor method for mean-flow angles $\theta = 0°$ (*top*), 30° (*middle*), and 270° (*bottom*) with respect to the main domain x-axis. *Left column:* Identification of inflow slabs (dashed coloured rectangles) in precursor domains ($x'y'$) and fringe slabs (full coloured rectangles) in main domain (xy: blue). *Middle and right column:* Remapping procedure of domain-crossing inflow slabs to single precursor domain using periodic boundary conditions.

direction. Because the precursor simulation runs concurrently with the main simulation, this rotation can happen during runtime without any a priori knowledge about the evolution of the mean-flow direction. That is to say, the rotation could be the outcome of a larger-scale simulation (e.g. a mesoscale simulation).

Figure 5 illustrates cases with a set of desired inflow angles inclined at $\theta = 0°$, 30°, and 210° with respect to the main domain of interest. Because the precursor

domain is doubly periodic, it can be continuously extended into an infinite amount of horizontally adjacent domain copies. Further, we use the convention that the mean flow in the precursor is oriented in the positive x' direction. The precursor domain is hypothetically attached to the main domain at an arbitrary reference hinge point, in the illustration the top left corners of both domains (from a top view perspective), with the freedom of rotating the precursor domain around it. Inflow conditions are provided to the fringe regions of the main simulation, indicated in the left column of Fig. 5 as ("*fringe slabs*"). To that end, flow-field data are extracted from the ("*inflow slabs*") in the precursor simulation, also marked in the figure. From the top row of Fig. 5, it can be seen that in the case of angle $\theta = 0^\circ$ these regions are located in the same place in both the main and precursor domain, hence the variable inflow direction concurrent precursor method becomes equivalent to the constant inflow angle method elaborated above in Sect. 4.1. In the general case, the discrete locations from which inflow conditions are to be extracted do not coincide with grid points of the precursor domain. Therefore a simple second-order bilinear interpolation scheme is applied. By extracting data from the dynamically moving inflow slabs, after multiplication with the classical rotation matrix

$$R_\theta = \begin{bmatrix} \cos\theta & -\sin\theta & 0 \\ \sin\theta & \cos\theta & 0 \\ 0 & 0 & 1 \end{bmatrix}, \tag{5}$$

inflow conditions can be derived for any given inflow angle θ.

The double periodicity of the precursor domain allows us to extract continuous inflow data from inflow slabs, even if they cross any of the horizontal domain boundaries. This is done by partitioning the inflow slab every time a domain boundary is crossed and afterwards reassembling all the regions in the correct order. This results in the complex arrangements of inflow slabs shown in the middle and right columns of Fig. 5. Finally, when mapping the inflow slabs to the fringe slabs, a discontinuity in the reference velocity for the fringe regions is introduced in the corner of the main domain, as values to the north and east of the corner are respectively copied from the south-east and north-west in the inflow slabs. However, with the use of smooth fringe forcing functions (Eq. 4b) applied to the ("*fringe corner*") region, this does not cause any issues in the simulations. Finally, note that the wide range of inflow angles illustrated in Fig. 5 illustrates that the proposed method does not have any restrictions on maximum/minimum angles, i.e. it can be used for any possible flow direction.

Figure 6 demonstrates the application of the method in a simulation for a flow angle of $\theta = 30^\circ$. It is observed that the fringe regions perform very well in forcing the flow field to the data extracted from the inflow slabs of the precursor simulation. Also, note the smooth transition between the precursor domain copies in the back and the main domain. Figure 7 further illustrates the dynamics of the method for a changing mean-flow direction, both seen from the precursor reference frame, and from the main reference frame.

The proposed approach is limited by the fact that the rotation of the main domain leads to time-varying locations of the inflow slabs in the precursor domain. This effect causes artificial compression or elongation of turbulent structures in the inflow conditions. The severity of this effect can be estimated based on the height-dependent ratio $\varphi(z) = \Omega L_h / U_h(z)$, which should be sufficiently low. In this relation, Ω is the instantaneous imposed rate of rotation of the inflow direction,

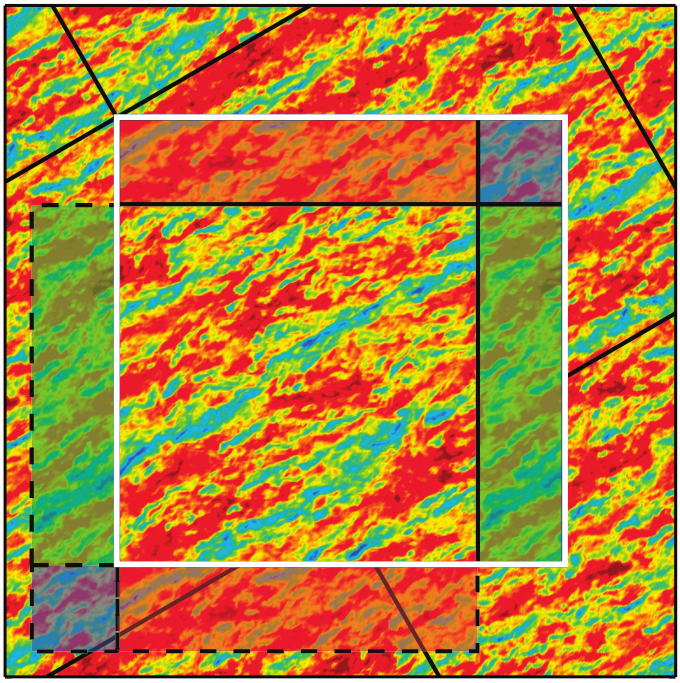

Fig. 6 Graphical illustration of variable inflow-direction precursor method showing contours of the horizontal velocity component in a neutral boundary layer. *Background*: tiled precursor domains (boundaries in black), rotated to desired inflow angle. *Foreground*: main domain (inside white frame). *Coloured patches*: fringe slabs (full lines) and inflow slabs (dashed lines). Corresponding slabs are indicated by matching face colours.

$L_h = (L_x^2 + L_y^2)^{1/2}$ is the horizontal diagonal length of the main domain and $U_h(z) = (u_x(z)^2 + u_y(z)^2)^{1/2} \approx u_x(z)$ is the mean horizontal velocity component at a distance z from the bottom boundary in the precursor domain.

In order to estimate acceptable values of the parameter φ, we illustrate the effect of the travelling motion of the inflow slabs qualitatively in Fig. 8 for several values of φ. The domain size of these simulations is $L_x \times L_y \times H = 2\pi \times 2\pi \times 1$ km^3. It can be observed in Fig. 8 that, for $\varphi \geq 1$, the turbulent structures become elongated and warped (especially visible in the left-bottom corner of the domain). The severity of this warping increases with increasing φ. It can therefore be concluded that this method is only applicable provided that the rate of change of imposed flow direction is not excessively fast compared to the time scales of the turbulence present in the flow. A conservative upper bound for sustained rotations can therefore be estimated to be $\varphi = 2/3$.

As a final note, we remark that the current methodology may not be the only feasible approach to generalize precursor methods for varying flow directions. In fact, in a first attempt, we focussed on varying the driving pressure gradient in the precursor domain. Such an approach has been employed for steady flow-direction simulations of an Ekman spiral by Sescu and Meneveau (2014), Allaerts and Meyers (2015), and Abkar and Porté-Agel (2015) to reorient the flow to a desired direction at a given height in the spiral. Unfortunately, in unsteady situations,

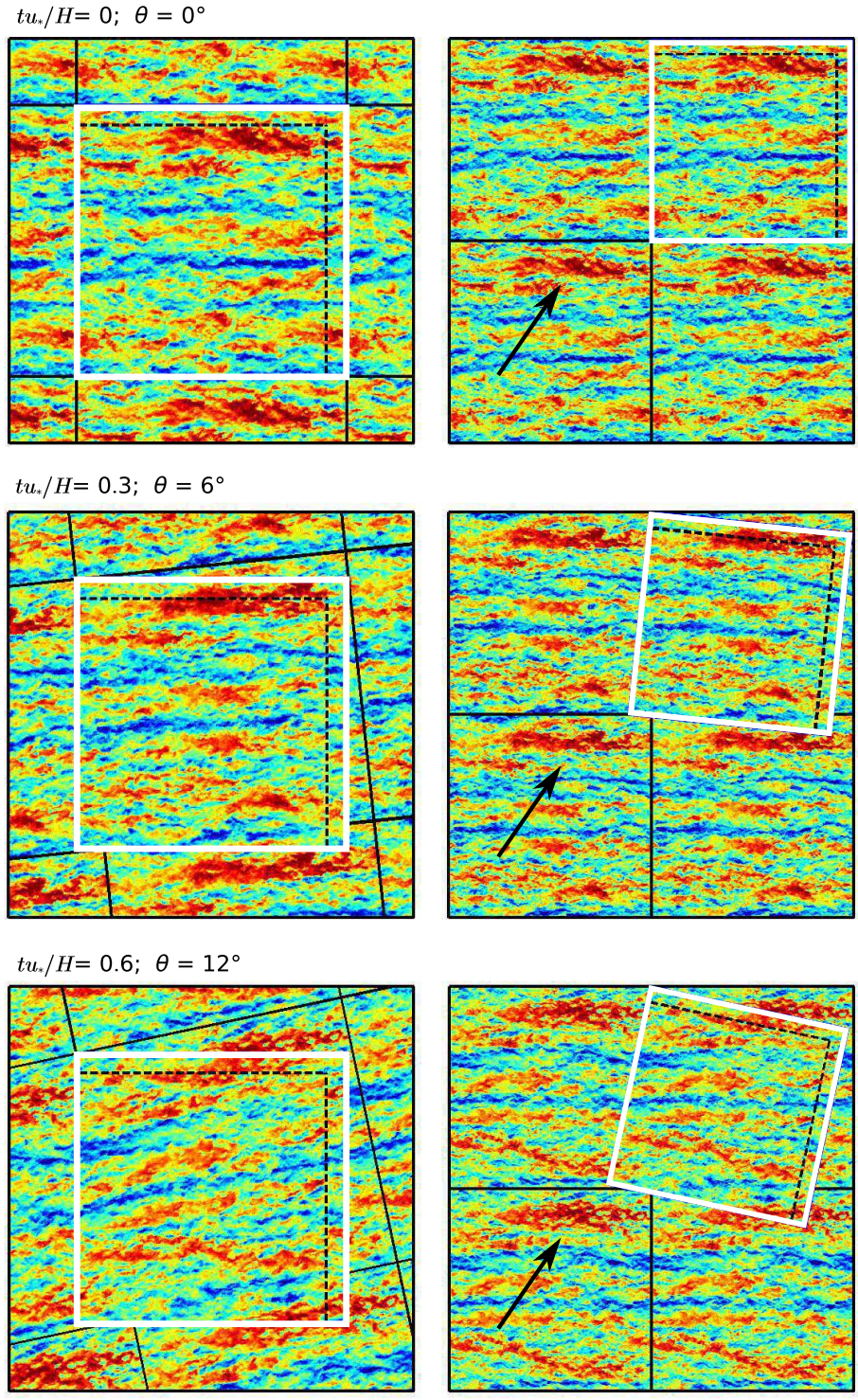

Fig. 7 Dynamic action of the variable inflow-direction precursor method with a time-varying mean-flow direction θ, as seen from two different reference frames. Colours show contours of the horizontal velocity component. *Left:* Stationary main domain (white with black dashed fringe regions), rotated background precursor domains. *Right:* Main domain, rotating around hinge point, on stationary background periodic precursor domains. Snapshots are separated in time by roughly one precursor flow-through time, as indicated by the black arrows pointing to a high speed flow region on the right panel in every snapshot.

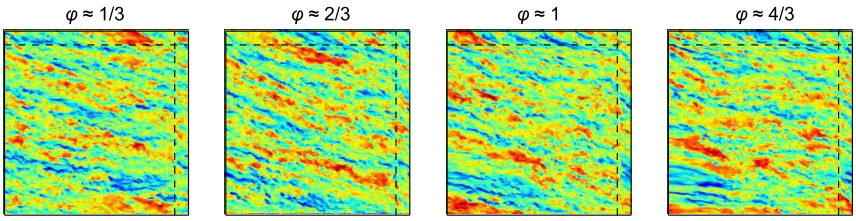

Fig. 8 Contours of the horizontal velocity component for different values of φ at a height $z/H = 0.1$. The imposed flow angle has been rotated to 30° with a constant rate of rotation Ω, varying between cases. The start of the fringe regions is indicated by the dashed black lines.

this leads to a large phase-lag between the pressure gradient and the mean-flow direction (that could be as long as hours), so that we did not further explore this route.

5 Horns Rev Wind-Farm Simulation

In this section the proposed concurrent precursor method is used in the context of a sample application where variability in inflow direction is particularly important. As mentioned before, such conditions are necessary in modelling wind farms placed in the ABL subjected to possible mesoscale variability. We illustrate the method for modelling a real wind farm, namely the Horns Rev offshore wind farm located about 15 km off the Danish western coast. This wind farm has been subject to many research studies, both numerical and experimental (see, e.g., Barthelmie et al. 2007; Peña and Hahmann 2012; Hansen et al. 2012; Porté-Agel et al. 2013).

5.1 Case Description And Numerical Setup

The farm consists of 80 Vestas V80-2MW turbines with a hub height of $z_h = 70$ m and a rotor diameter $D = 80$ m. The simulation domain is illustrated in Fig. 9. The turbines are laid out as an oblique rectangle of 10 rows by 8 columns, sheared with approximately 7° with respect to the north-south line. Here, we refer to a group of turbines located on the same east-west line as a column. Likewise, a group of turbines on a north-south line (with a 7° angle) is denoted as a row. Turbines are spaced apart approximately $7D$ in both the streamwise (east-west) and spanwise (north-south) direction. The turbines are represented in the simulation using an ADM (see Sect. 2) with $C_T' = 1.53$, corresponding to a thrust coefficient $C_T = 0.78$ (see, e.g., Wu and Porté-Agel 2015; Stevens et al. 2015). The dimensions of the main simulation domain are $L_x = L_y = 10$ km in the horizontal directions and $L_z = 1$ km in the vertical direction. This relatively large domain rules out any possible upstream influence of the fringe regions on the farm (Lundbladh et al. 1999; Nordström et al. 1999).

A uniform grid of $768 \times 768 \times 192$ grid points is used in the main domain, and the same grid size is used for the precursor domain. This leads to a resolution of $\Delta_x = \Delta_y = 13$ m in the horizontal directions and $\Delta_z = 5.21$ m in the vertical direction. The timestep is restricted by the advective Courant–Friedrichs–Lewy

number, and fluctuates around 0.6 seconds. Inflow conditions are generated by a parallel auxiliary precursor simulation, as discussed in previous sections. Details of the case setup are further summarized in Table 1.

In the simulations, the turbines are yawed in response to the incident flow angle. The yaw controller is based on the heuristic baseline controller developed by Kooijman et al. (2003), and later successfully applied by Storey et al. (2014) in wind-farm LES. Whenever 90 s or 5 s running average yaw errors exceed 5° or 30° respectively, the turbine starts yawing at a constant speed of 0.1°/sec to compensate the offset, until the 5 s yaw error drops below 0.5°.

Simulation results are dimensionalized with the domain height $H = 1000$ m and a friction velocity of $u_* = 0.357$ m s^{-1}. This leads to a wind speed of approximately 8 m s^{-1} at hub height ($z_h = 70$ m), upstream of the farm. In this study, we select a roughness length $z_0 = 0.01$ m. Even though this value is significantly higher than the roughness length observed in typical offshore conditions, the resulting observed turbulence intensity (TI) at hub height is approximately 7.5%. This is close to prior numerical studies (Porté-Agel et al. 2013; Wu and Porté-Agel 2015) and experimental observations (Barthelmie et al. 2009, 2010) for the Horns Rev wind farm, where TI was found to be less than 8% for neutral atmospheric conditions. TI is defined here as $(\langle \overline{u_i' u_i'} \rangle / 3)^{1/2} / \langle \overline{u}_{hub} \rangle$, where brackets and overline denote horizontal and time-averaging operators respectively.

First, a statistically steady turbulent boundary layer is created by spinning up the precursor simulation from random perturbations for a time period corresponding to slightly over 20 physical hours. Afterwards, the generated field is used in both the precursor and main simulation domain. The turbines are then inserted in the main domain, and the flow is further advanced in time for roughly 1 h, so that the wind farm in the main domain also attains statistical equilibrium. This point in time is denoted as $t = 0$ in all figures and discussion.

We consider a set of simulations in which the mean wind direction is varied sinusoidally in time as $\theta(t) = 270° - 30° \sin(2\pi t / T_\theta)$, where the period of the sine wave T_θ equals 1 h (Case V1), 2 h (Case V2), and 4 h (Case V4). Moreover, we define a set of reference cases with a steady mean wind direction in the sector around the 270° (westerly) wind direction. This set consists of 15 separate LES for mean wind directions as indicated in Table 1, and are referred to as ST hereafter. Cases V1, V2, V4 and ST270 are simulated for a time horizon of 4 h, whereas the other steady cases (ST) are performed for a period of 2 h. For the variable cases V4, V2, and V1, the imposed rotation rates lead to average ratios φ of approximately 0.25, 0.5, and 1, respectively. Note that, for Case V1, φ is higher than our conservative upper bound estimate of 2/3 (see further discussion below).

5.2 Results

First a set of steady cases (ST) in a sector around the 270° wind direction is discussed, and compared to experimental and simulation data from literature. Results of variable wind-direction cases (V) are presented afterwards. Figure 10 shows the extracted power for a 270° mean wind direction, obtained from Case ST270, averaged over each turbine row and normalized by the first row. This particular wind direction is well documented in literature, with experimental power measurements from the SCADA data of the Horns Rev wind farm (Barthelmie et al. 2009, 2010).

Domain size (km^3)	$L_x \times L_y \times H = 10 \times 10 \times 1$
Turbine dimensions (m)	$D = 80$, $z_h = 70$
Turbine arrangement	10 (E-W) $\times$8 (N-S) (see Fig. 9)
Turbine spacing	$S_x = 7D$ (E-W), $S_y = 6.95D$ (N-S)
Surface roughness (m)	0.01
Grid size in main//precursor	$N_x \times N_y \times N_z = 768 \times 768 \times 192$ // $768 \times 768 \times 192$
Cell size (m^3)	$\Delta_x \times \Delta_y \times \Delta_z \approx 13 \times 13 \times 5.2$
Timestep (s)	≈ 0.6
Wind direction: steady (ST)	$\theta = 270°$, 271°, 273°, 275°, 280°, 285°, 290°, 300°, 269°, 267°, 265°, 260°, 255°, 250°, 240°
Wind direction: time-varying (V)	$\theta = 270° - 30° \sin(2\pi t/T_\theta)$ T_θ = 1h (V1), 2h (V2), 4h (V4)

Table 1 Summary of simulation setup parameters.

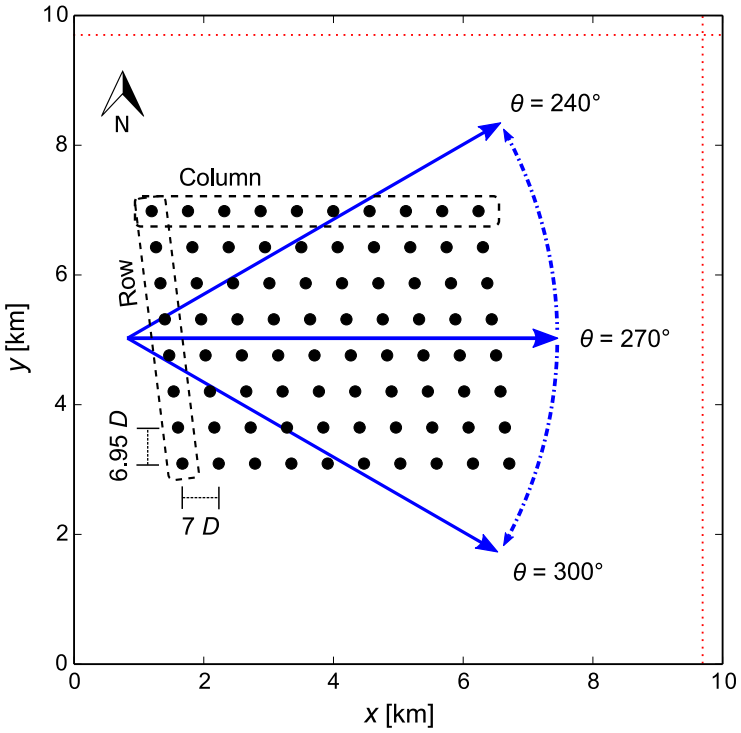

Fig. 9 Simulation domain for Horns Rev wind farm. The location of the turbines is indicated with black circles. The dashed-red lines indicate the start of the fringe regions.

Previous LES results are also shown (Ivanell 2009; Porté-Agel et al. 2013). It is appreciated in Fig. 10 that our simulation results show relatively good agreement with the experimental data, as well as with the LES data from Porté-Agel et al. (2013). The main discrepancies with the latter occur in the entrance region of the wind farm, i.e. in the second and third rows. This is related to the use of a different subgrid-scale model, and a different ADM in our code: Porté-Agel et al. (2013) use a scale-dependent dynamic Smagorinsky model which is known to be less dissipative than our standard Smagorinsky model. They further also use a

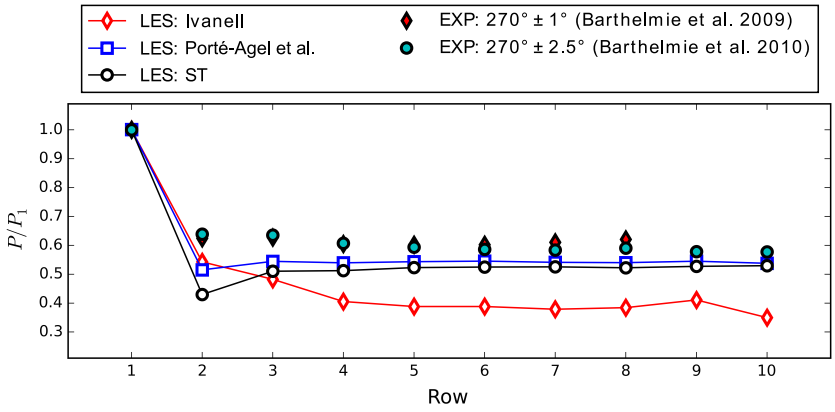

Fig. 10 Normalized power as a function of row number. Numerical reference data from Ivanell (2009) and Porté-Agel et al. (2013), and experimental measurements from Barthelmie et al. (2009, 2010) are included.

more advanced rotating actuator disk implementation. Further downstream, our results closely match results of Porté-Agel et al. (2013), as well as the Horns Rev measurement data. For sake of reference, the results reported by Ivanell (2009) are also included in Fig. 10. These results were obtained using the Mann spectral model for the generation of inflow turbulence, and it is appreciated that this leads to a significant underprediction of power extraction. Later, this was attributed to a decreased triggering of wake meandering by Mann turbulence compared to precursor generated turbulence (Churchfield et al. 2012b).

Figure 11 shows top views of the flow field for the different variable wind-direction cases (V1, V2, V4) at different time instances to illustrate the flow behaviour for different wind directions. As can be expected, the distance over which the wakes are able to recover before they hit the next turbines changes significantly with wind direction. Further focussing on Case V1, for which $\varphi \approx 1$ is slightly too high compared to our estimated upper limit $\varphi \leq 2/3$ in Sect. 4.2, we do not observe the type of severe distortions of turbulent structures that we found earlier in Fig. 8 for too high rotation rates. However, when looking at the full range of snapshots for this case (not shown here), distortions are sometimes visible for short times near the edges of the computational domain, but they do not seem to affect the main features of the flow in the wind farm itself. This confirms however the estimate $\varphi \leq 2/3$ discussed in Sect. 4.2.

Figure 12 contains a summary of simulation results for the variable wind-direction cases (V). From the top row, it can be appreciated that the mean yaw angle in the wind farm follows the imposed wind direction closely for all cases, although some overshoots are observed for Case V1. The middle row shows aggregate power output as a function of time, combined with Case ST270. The increased variability of aggregate farm power for the variable wind-direction cases is mainly caused by the strong sensitivity of power extraction on mean wind direction, as is well known from previous studies (see, e.g. Barthelmie et al. 2010; Porté-Agel et al. 2013). Moreover, it is shown that cases V1 and V2 exhibit significant hysteresis effects, i.e. the waveforms of aggregate power show a strong asymmetry

with leading peaks. Case V4, which is subject to slower variations, shows a more symmetric pattern.

The bottom row of Fig. 12 shows aggregate power as a function of mean wind direction. Time-averaged wind-farm power extractions obtained from the steady wind-direction cases (ST) are also shown. As may be expected, time-varying simulation results increasingly correspond to steady state cases when the rate of rotation is decreased. However, the hysteresis effects of the faster rotation cases are also clearly visible. Moreover, all cases show significant undershoots in power extraction around the fully-waked 270° conditions. This is further explained based on Fig. 13 for Case V2. The figure compares an instantaneous flow field from a steady 270° simulation to the 270° solution from the unsteady case after 4 h. It is observed that in the steady wind-direction simulation, high-speed channels in between the turbine columns are much more pronounced and penetrate much deeper into the farm. This can be explained by the changing wind direction in the variable case, which much better mixes the high-speed regions with the low speed regions between the turbines. As a result, at an earlier stage in the simulation ($\theta \neq 270°$) the available inflow energy in the farm was better captured by the first rows of turbines, leaving less energy in the 'high-speed' channels near the end of the farm at the later $\theta = 270°$ instance. The reduced power extraction for the variable cases at 270° (observed in Fig. 12) is a result of this process.

Figure 14 shows time spectra ϕ of the aggregate wind-farm power for Case ST270, V1, V2, and V4. It is observed for frequencies higher than 0.02 Hz that all cases show identical spectral behaviour. Results show a Kolmogorov-type $-5/3$ scaling range, which transitions to a -1 range at lower frequencies. Moreover, the spectrum of Case ST270 exhibits a spectral peak in the frequency range around 10^{-2} Hz, which is directly related to the time for the flow to proceed from one row of turbines to the next. The existence of the peak is caused by the correlation between extracted power of turbines within the same column, which in turn is due to the advection of large-scale streamwise-oriented turbulent structures. For a more detailed analysis of this phenomenon, we refer the reader to Stevens and Meneveau (2014). In the variable wind-direction cases, the peak is smeared out as here the turbine-to-turbine flow time no longer corresponds to a narrow frequency band. These cases also exhibit increased energy at the low frequency part of the spectrum, caused by the single-frequency variation in wind direction. This is also shown in the time series of aggregate farm power in Fig. 12.

In summary, the current section provides a demonstration case for the proposed variable inflow-direction concurrent precursor method. A set of steady state reference cases at different wind directions is defined with the aim of illustrating hysteresis effects in power extraction for the variable wind-direction cases. As the rate of rotation is decreased, the latter show increased correspondence with the reference cases. However, even Case V4, which exhibits the slowest variations, displays an undershoot at $\theta = 270°$, compared to the steady state Case ST270. Even though time series of extracted farm power appear very different qualitatively, spectral behaviour at higher frequencies is found to be identical.

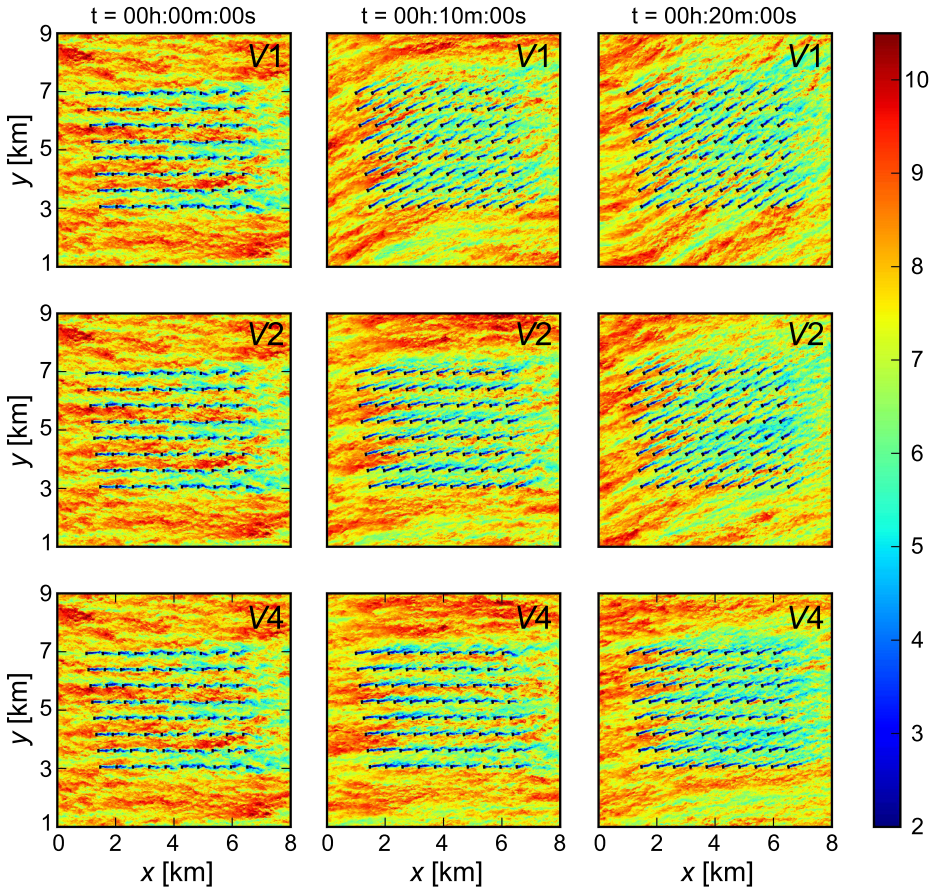

Fig. 11 Plan view of instantaneous flow field at hub height for variable wind-direction cases at three time instances visualized using contours of the horizontal velocity component. *Top:* V1. *Middle:* V2. *Bottom:* V4. The units on the colour bar are m s^{-1}.

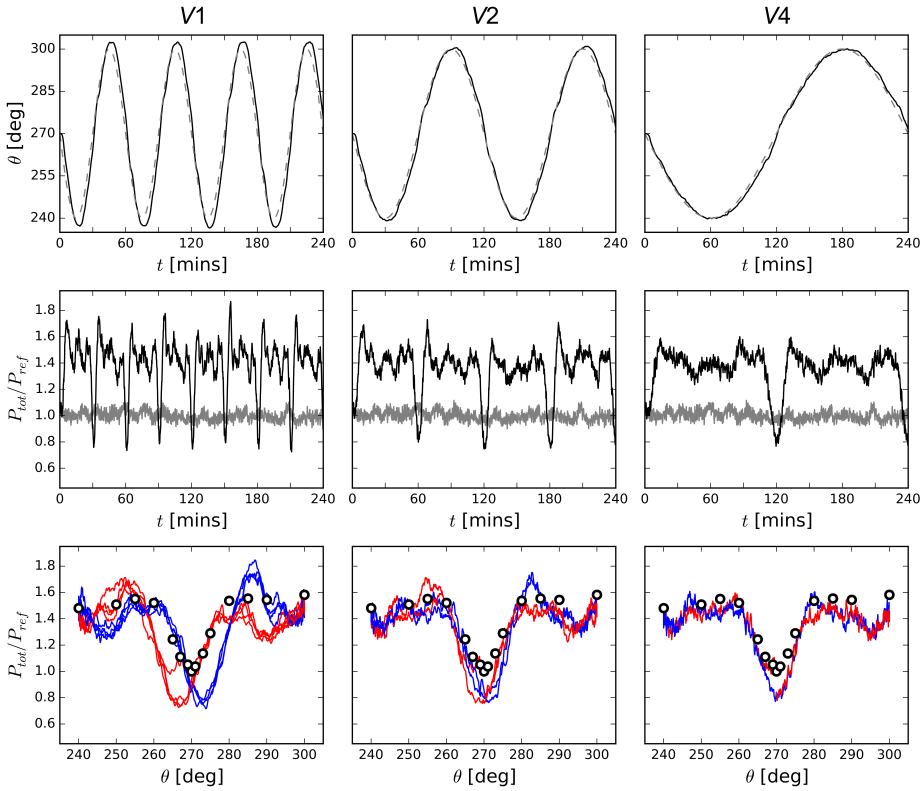

Fig. 12 Simulation results for Case V1 (*left*), V2 (*middle*), and V4 (*right*). *Top*: Imposed wind direction (dashed lines) and resulting mean turbine yaw angle (full lines). *Middle*: Aggregate wind-farm power extraction, along with Case ST270, normalized by time-averaged ST270 power. *Bottom:* Aggregate wind-farm power extraction as a function of mean-flow angle for the time-varying wind direction cases (lines), as well as a set of steady state cases at several mean-flow angles (circles). Red and blue lines indicate time periods during which $d\theta/dt > 0$, and $d\theta/dt < 0$ respectively. Power is normalized by time-averaged ST270 power.

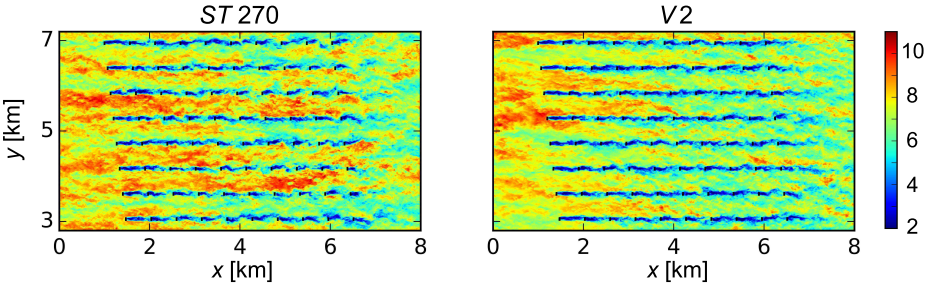

Fig. 13 Contours of the instantaneous horizontal velocity component at turbine hub height for $\theta = 270°$. *Left:* Steady state case ST270. *Right:* Variable wind-direction case V2 at $t =$ 4 h.

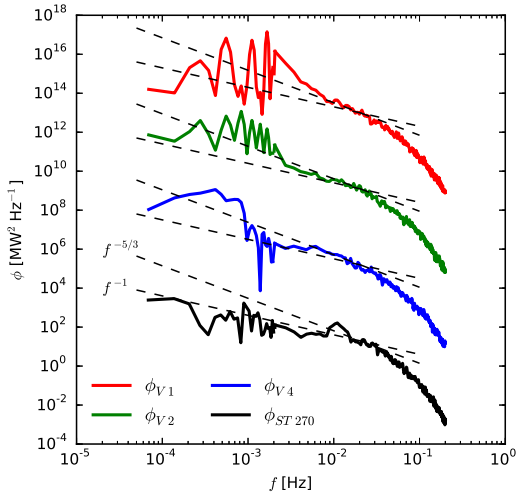

Fig. 14 Time spectra of extracted power ϕ for cases ST270, V1, V2, and V4. Cases shifted vertically for clarity of presentation. Spectra for frequencies $f > 2 \times 10^{-3}$ Hz are calculated using Welch's periodogram method for better statistical convergence.

6 Conclusions

We have addressed the long-standing issue of the generation of inflow conditions for turbulence-resolving flow simulations. The importance of high quality inflow turbulence has been reaffirmed based on a literature review and presentation of a qualitative comparison between precursor methods and a sample of synthetic inflow methods. While precursor techniques are the only methods capable of producing large-scale coherent structures and display the best quality overall, classical implementations lack the flexibility to apply them to flow cases involving variable mean inflow directions. To circumvent this limitation, a variable-direction precursor method has been developed and implemented in the SP-Wind LES solver (Meyers and Meneveau 2010). The approach can provide fully developed turbulent inflow conditions to turbulence-resolving simulations for variable mean-flow directions at a computational cost that does not exceed the cost of classical precursor techniques. The method is relatively general as it can be applied to LES or DNS whenever variable inflow conditions are prescribed, provided the rate of change of imposed flow direction is not excessively fast compared to the time scales of the turbulence in the main domain of interest.

The proposed method was applied to a set of three LES of the Horns Rev wind farm, subject to an imposed hypothetical sinusoidal variation in wind direction with an amplitude of $\pm 30^\circ$ and time periods of 1, 2, and 4 h respectively. A comparison with steady state simulations illustrated that the cases with 1 and 2 h periods exhibit significant hysteresis effects in power extraction. Moreover, all variable wind-direction simulation cases show an undershoot of power production at westerly flow, compared to steady-state conditions. Finally, even though time series of extracted power appear very different qualitatively, spectral behaviour at higher frequencies was found to be identical.

In the current work, we developed a precursor method that supports time-varying inflow directions. However, there exists a range of other atmospheric phenomena such as coherent gusts, mean wind convergence, and updrafts or downdrafts that can also have an important impact on microscale boundary conditions. Including them in a further generalization of the precursor method is an interesting topic for future research.

Acknowledgements We thank Dr. R. Stevens for useful discussions. WM and JM acknowledge support by the ERC (ActiveWindFarms, grant no: 306471). CM acknowledges support by the NSF (grant IIA-1243482, the WINDINSPIRE project). The computational resources and services used in this work were provided by the VSC (Flemish Supercomputer Center), funded by the Hercules Foundation and the Flemish Government - department EWI.

References

Abkar M, Porté-Agel F, (2015) A new wind-farm parameterization for large-scale atmospheric models. J Renewable Sustainable Energy 7(1):013121

Albertson JD, Parlange MB (1999) Surface length scales and shear stress: Implications for land-atmosphere interaction over complex terrain. Water Resour Res 35(7):2121–2132

Allaerts D, Meyers J (2015) Large eddy simulation of a large wind-turbine array in a conventionally neutral atmospheric boundary layer. Phys Fluids 27(6):065108

682 Anderson W, Passalacqua P, Porté-Agel F, Meneveau C (2012) Large-eddy sim-
683 ulation of atmospheric boundary-layer flow over fluvial-like landscapes using a
684 dynamic roughness model. Boundary-Layer Meteorol 144(2):263–286
685 Araya G, Jansen KE, Castillo L (2009) Inlet condition generation for spatially
686 developing turbulent boundary layers via multiscale similarity. J Turbul 10:1–
687 33
688 Araya G, Castillo L, Meneveau C, Jansen K (2011) A dynamic multi-scale ap-
689 proach for turbulent inflow boundary conditions in spatially developing flows. J
690 Fluid Mech 670:581–605
691 Barthelmie RJ, Rathmann O, Frandsen ST, Hansen K, Politis E, Prospathopoulos
692 J, Rados K, Cabezón D, Schlez W, Phillips J, Neubert A, Schepers JG, van der
693 Pijl SP (2007) Modelling and measurements of wakes in large wind farms. In:
694 J. Phys.: Conference Series, IOP Publishing, vol 75, p 012049
695 Barthelmie RJ, Hansen K, Frandsen ST, Rathmann O, Schepers J, Schlez W,
696 Phillips J, Rados K, Zervos A, Politis E, Chaviaropoulos PK (2009) Modelling
697 and measuring flow and wind turbine wakes in large wind farms offshore. Wind
698 Energy 12(5):431–444
699 Barthelmie RJ, Pryor S, Frandsen ST, Hansen KS, Schepers J, Rados K, Schlez
700 W, Neubert A, Jensen L, Neckelmann S (2010) Quantifying the impact of wind
701 turbine wakes on power output at offshore wind farms. J Atmos Ocean Technol
702 27(8):1302–1317
703 Bou-Zeid E, Meneveau C, Parlange M (2005) A scale-dependent Lagrangian dy-
704 namic model for large eddy simulation of complex turbulent flows. Phys Fluids
705 17(2):025105
706 Bou-Zeid E, Parlange MB, Meneveau C (2007) On the parameterization of surface
707 roughness at regional scales. J Atmos Sci 64(1):216–227
708 Breton SP, Nilsson K, Olivares-Espinosa H, Masson C, Dufresne L, Ivanell S (2014)
709 Study of the influence of imposed turbulence on the asymptotic wake deficit in
710 a very long line of wind turbines. Renew Energ 70:153 – 163
711 Cal RB, Lebrón J, Castillo L, Kang HS, Meneveau C (2010) Experimental study of
712 the horizontally averaged flow structure in a model wind-turbine array boundary
713 layer. J Renewable Sustainable Energy 2(1):013106
714 Calaf M, Meneveau C, Meyers J (2010) Large eddy simulation study of fully de-
715 veloped wind-turbine array boundary layers. Phys Fluids 22(1):015110
716 Calaf M, Parlange MB, Meneveau C (2011) Large eddy simulation study of scalar
717 transport in fully developed wind-turbine array boundary layers. Phys Fluids
718 23(12):126603
719 Canuto C, Hussaini MY, Quarteroni A, Zang TA (1988) Spectral Methods in Fluid
720 Dynamics. Springer-Verlag, New York, NY, 567 pp
721 Churchfield MJ, Lee S, Michalakes J, Moriarty PJ (2012a) A numerical study of
722 the effects of atmospheric and wake turbulence on wind turbine dynamics. J
723 Turbul 13:1 – 32
724 Churchfield MJ, Lee S, Moriarty PJ, Martinez LA, Leonardi S, Vijayakumar G,
725 Brasseur JG (2012b) A large-eddy simulation of wind-plant aerodynamics. In:
726 Proceedings of 50th AIAA Aerospace Sciences Meeting including the New Hori-
727 zons Forum and Aerospace Exposition
728 Dietzel D, Messig D, Piscaglia F, Montorfano A, Olenik G, Stein OT, Kronenburg
729 A, Onorati A, Hasse C (2014) Evaluation of scale resolving turbulence generation
730 methods for large eddy simulation of turbulent flows. Comput Fluids 93:116 –

731 128
732 España G, Aubrun S, Loyer S, Devinant P (2011) Spatial study of the wake mean-
733 dering using modelled wind turbines in a wind tunnel. Wind Energy 14(7):923–
734 937
735 Ferrante A, Elghobashi S (2004) A robust method for generating inflow condi-
736 tions for direct simulations of spatially-developing turbulent boundary layers. J
737 Comput Phys 198(1):372–387
738 Garratt JR (1994) The atmospheric boundary layer. Cambridge University Press,
739 Cambridge, UK, 316 pp
740 Gilling L (2009) Tugen - synthetic turbulence generator manual and user's guide.
741 Tech. rep., Aalborg University, Aalborg, Denmark
742 Gilling L, Sørensen NN (2011) Imposing resolved turbulence in CFD simulations.
743 Wind Energy 14(5):661–676
744 Goit JP, Meyers J (2015) Optimal control of energy extraction in wind-farm bound-
745 ary layers. J Fluid Mech 768:5–50
746 Gopalan H, Gundling C, Brown K, Roget B, Sitaraman J, Mirocha JD, Miller WO
747 (2014) A coupled mesoscale–microscale framework for wind resource estimation
748 and farm aerodynamics. J Wind Eng Ind Aerodyn 132:13–26
749 Hansen KS, Barthelmie RJ, Jensen LE, Sommer A (2012) The impact of turbu-
750 lence intensity and atmospheric stability on power deficits due to wind turbine
751 wakes at Horns Rev wind farm. Wind Energy 15(1):183–196
752 International Electrotechnical Comission (2005) IEC 61400-1 standard. Wind tur-
753 bines - part 1: design requirements
754 Ivanell S (2009) Numerical computation of wind turbine wakes. PhD thesis, KTH
755 Mechanics, Royal Institute of Technology
756 Keating A, Piomelli U, Balaras E, Kaltenbach HJ (2004) A priori and a posteriori
757 tests of inflow conditions for large-eddy simulation. Phys Fluids 16(12):4696–
758 4712
759 Keck RE, Mikkelsen R, Troldborg N, Maré M, Hansen KS (2013) Synthetic at-
760 mospheric turbulence and wind shear in large eddy simulations of wind turbine
761 wakes. Wind Energy 17:1247 – 1267
762 Keylock C, Tokyay T, Constantinescu G (2011) A method for characterising the
763 sensitivity of turbulent flow fields to the structure of inlet turbulence. J Turbul
764 12:1 – 30
765 Klein M, Sadiki A, Janicka J (2003) A digital filter based generation of inflow data
766 for spatially developing direct numerical or large eddy simulations. J Comput
767 Phys 186(2):652–665
768 Kooijman H, Lindenburg C, Winkelaar D, van der Hooft E (2003) DOWEC 6
769 MW pre-design. Tech. Rep. ECN-CX-01-125, Energy Research Center of the
770 Netherlands, Petten, the Netherlands
771 van der Laan M, Storey R, Norris S, Cater J, et al. (2014) A CFD code comparison
772 of wind turbine wakes. In: J. Phys.: Conference Series, IOP Publishing, vol 524,
773 p 012140
774 Lu H, Porté-Agel F (2011) Large-eddy simulation of a very large wind farm in a
775 stable atmospheric boundary layer. Phys Fluids 23(6):065101
776 Lund TS, Wu X, Squires KD (1998) Generation of turbulent inflow data for
777 spatially-developing boundary layer simulations. J Comput Phys 140(2):233–
778 258

Lundbladh A, Berlin S, Skote M, Hildings C, Choi J, Kim J, Henningson DS (1999) An efficient spectral method for a simulation of incompressible flow over a flat plate. Trita-mek Tech Rep: 11 KTH

Mann J (1998) Wind field simulation. Probabilist Eng Mech 13(4):269–282

Mason PJ, Thomson D (1992) Stochastic backscatter in large-eddy simulations of boundary layers. J Fluid Mech 242:51–78

Mayor SD, Spalart PR, Tripoli GJ (2002) Application of a perturbation recycling method in the large-eddy simulation of a mesoscale convective internal boundary layer. J Atmos Sci 59(15):2385–2395

Mehta D, Van Zuijlen A, Koren B, Holierhoek J, Bijl H (2014) Large eddy simulation of wind farm aerodynamics: A review. J Wind Eng Ind Aerodyn 133:1–17

Meyers J, Meneveau C (2010) Large eddy simulations of large wind-turbine arrays in the atmospheric boundary layer. AIAA Paper 827:2010

Meyers J, Meneveau C (2013) Flow visualization using momentum and energy transport tubes and applications to turbulent flow in wind farms. J Fluid Mech 715:335–358

Meyers J, Sagaut P (2007) Evaluation of Smagorinsky variants in large-eddy simulations of wall-resolved plane channel flows. Phys Fluids 19(9):095105

Mikkelsen R (2003) Actuator disc methods applied to wind turbines. PhD thesis, Technical University of Denmark

Mirocha J, Kosovic B, Aitken M, Lundquist J (2014a) Implementation of a generalized actuator disk wind turbine model into the weather research and forecasting model for large-eddy simulation applications. J Renewable Sustainable Energy 6(1):013104

Mirocha J, Kosović B, Kirkil G (2014b) Resolved turbulence characteristics in large-eddy simulations nested within mesoscale simulations using the weather research and forecasting model. Mon Weather Rev 142(2):806–831

Moeng CH (1984) A large-eddy-simulation model for the study of planetary boundary-layer turbulence. J Atmos Sci 41(13):2052–2062

Muñoz-Esparza D, Kosović B, van Beeck J, Mirocha J (2015) A stochastic perturbation method to generate inflow turbulence in large-eddy simulation models: Application to neutrally stratified atmospheric boundary layers. Phys Fluids 27(3):035102

Nordström J, Nordin N, Henningson D (1999) The fringe region technique and the Fourier method used in the direct numerical simulation of spatially evolving viscous flows. SIAM J Sci Comput 20(4):1365–1393

Orlanski I (1975) A rational subdivision of scales for atmospheric processes. Bull Am Meteorol Soc 56:527–530

Park J, Basu S, Manuel L (2014) Large-eddy simulation of stable boundary layer turbulence and estimation of associated wind turbine loads. Wind Energy 17(3):359–384

Peña A, Hahmann AN (2012) Atmospheric stability and turbulence fluxes at Horns Rev - an intercomparison of sonic, bulk and WRF model data. Wind Energy 15(5):717–731

Piomelli U, Balaras E (2002) Wall-layer models for large-eddy simulations. Annu Rev Fluid Mech 34(1):349–374

Porté-Agel F, Wu YT, Lu H, Conzemius RJ (2011) Large-eddy simulation of atmospheric boundary layer flow through wind turbines and wind farms. J Wind Eng Ind Aerodyn 99(4):154–168

828 Porté-Agel F, Wu YT, Chen CH (2013) A numerical study of the effects of wind
829 direction on turbine wakes and power losses in a large wind farm. Energies
830 6(10):5297–5313
831 Rana Z, Thornber B, Drikakis D (2011) On the importance of generating accurate
832 turbulent boundary condition for unsteady simulations. J Turbul 12:1–39
833 Ray PS (1986) Mesoscale meteorology and forecasting. American Meteorological
834 Society, Boston, MA, 793 pp
835 Sarlak H, Meneveau C, Sørensen JN (2015) Role of subgrid-scale modeling in large
836 eddy simulation of wind turbine wake interactions. Renew Energ 77:386–399
837 Schlatter P, Adams N, Kleiser L (2005) A windowing method for periodic
838 inflow/outflow boundary treatment of non-periodic flows. J Comput Phys
839 206(2):505–535
840 Sescu A, Meneveau C (2014) A control algorithm for statistically stationary large-
841 eddy simulations of thermally stratified boundary layers. Q J R Meteorol Soc
842 140(683):2017–2022
843 Shur ML, Spalart PR, Strelets MK, Travin AK (2014) Synthetic turbulence gener-
844 ators for RANS-LES interfaces in zonal simulations of aerodynamic and aeroa-
845 coustic problems. Flow Turbul Combust 93(1):63–92
846 Smagorinsky J (1963) General circulation experiments with the primitive equa-
847 tions: I. the basic experiment. Mon Weather Rev 91(3):99–164
848 Spalart PR (1988) Direct simulation of a turbulent boundary layer up to $R_\theta =$
849 1410. J Fluid Mech 187:61–98
850 Spalart PR, Watmuff JH (1993) Experimental and numerical study of a turbulent
851 boundary layer with pressure gradients. J Fluid Mech 249:337–371
852 Stevens RJAM, Meneveau C (2014) Temporal structure of aggregate power fluc-
853 tuations in large-eddy simulations of extended wind-farms. J Renewable Sus-
854 tainable Energy 6(4):043102
855 Stevens RJAM, Gayme DF, Meneveau C (2014a) Large eddy simulation studies of
856 the effects of alignment and wind farm length. J Renewable Sustainable Energy
857 6(2):023105
858 Stevens RJAM, Graham J, Meneveau C (2014b) A concurrent precursor inflow
859 method for large eddy simulations and applications to finite length wind farms.
860 Renew Energ 68:46–50
861 Stevens RJAM, Gayme DF, Meneveau C (2015) Using the coupled wake boundary
862 layer model to evaluate the effect of turbulence intensity on wind farm perfor-
863 mance. J. Phys.: Conference Series 625(1):012004
864 Storey R, Norris S, Stol K, Cater J (2013) Large eddy simulation of dynamically
865 controlled wind turbines in an offshore environment. Wind Energy 16(6):845–
866 864
867 Storey R, Norris S, Cater J (2014) Modelling turbine loads during an extreme
868 coherent gust using large eddy simulation. In: J. Phys.: Conference Series, IOP
869 Publishing, vol 524, p 012177
870 Stull RB (1988) An introduction to boundary layer meteorology, Kluwer Acad.
871 Publ., Dordrecht, 670 pp
872 Tabor G, Baba-Ahmadi M (2010) Inlet conditions for large eddy simulation: a
873 review. Comput Fluids 39(4):553–567
874 Troldborg N, Larsen GC, Madsen HA, Hansen KS, Sørensen JN, Mikkelsen R
875 (2011) Numerical simulations of wake interaction between two wind turbines at
876 various inflow conditions. Wind Energy 14(7):859–876

877 Verstappen R, Veldman A (2003) Symmetry-preserving discretization of turbulent
878 flow. J Comput Phys 187(1):343–368
879 Vincent CL (2010) Mesoscale wind fluctuations over Danish waters. PhD thesis,
880 Technical University of Denmark
881 Wan F, Porté-Agel F (2011) A large-eddy simulation study of turbulent flow over
882 multiscale topography. Boundary-Layer Meteorol 141(2):201–217
883 Wu YT, Porté-Agel F (2011) Large-eddy simulation of wind-turbine wakes: eval-
884 uation of turbine parametrisations. Boundary-Layer Meteorol 138(3):345–366
885 Wu YT, Porté-Agel F (2012) Atmospheric turbulence effects on wind-turbine
886 wakes: An LES study. Energies 5(12):5340–5362
887 Wu YT, Porté-Agel F (2013) Simulation of turbulent flow inside and above
888 wind farms: Model validation and layout effects. Boundary-Layer Meteorol
889 146(2):181–205
890 Wu YT, Porté-Agel F (2015) Modeling turbine wakes and power losses within a
891 wind farm using LES: An application to the Horns Rev offshore wind farm.
892 Renew Energ 75:945 – 955